Mode competition of the vortex-induced vibration for the long-span bridges with the closely-spaced multi-modes

Wei Cui · Liutian Zhang · Lin Zhao

Abstract In recent years, vortex-induced vibration (VIV) phenomena have been observed in various long-span bridges worldwide. The existing literature has presented several nonlinear mathematical models for VIV, predominantly founded on a single dynamic mode. However, long-span bridges inherently possess multiple modes, and with the expansion of bridge spans, the frequencies associated with these structural modes become closely spaced. The incongruity arises from the linear assumption inherent in dynamic mode decomposition and the nonlinear dynamics characterizing VIV, thereby impeding the extrapolation of single-mode VIV to scenarios involving multiple coupled modes. This research introduces a multimode VIV modeling approach to emulate the coupling effects among modes. The equations governing the multimode amplitudes evolution during VIV are derived through averaging methods. In particular, the multi-mode VIV model can be reduced to a conventional single-mode VIV model, facilitating the identification of aeroelastic parameters during VIV through wind tunnel testing. The investigation reveals that coupled multimode VIV consistently converges towards a stable equilibrium point corresponding to a single mode after modes undergo competition. Finally, this article concludes with a discussion on the influence of structural damping on coupled multimode VIV.

W. Cui · L. Zhang · L. Zhao
State Key Lab of Disaster Reduction in Civil Engineering, Tongji University, 1239 Siping Road, Shanghai 200092, China
e-mail: cuiwei@tongji.edu.cn

L. Zhang
e-mail: zlt@tongji.edu.cn

W. Cui · L. Zhao
Key Laboratory of Transport Industry of Wind Resistant Technology for Bridge Structures, Tongji University, 1239 Siping Road, Shanghai 200092, China

L. Zhao (✉)
College of Civil Engineering and Architecture, Guangxi University, 100 Eastern Daxue Road, Nanning 530004, Guangxi, China
e-mail: zhaolin@tongji.edu.cn

1 Introduction

1.1 Vortex-induced vibration of long-span bridge

Vortex-induced vibration (VIV) is a major concern for long-span bridges in recent years [1]. There are several VIV events that occurred on super long-span bridges, such as the Deer Isle bridge in the USA [2], the Great Belt bridge in Denmark [3,4], the Trans-Tokyo Bay crossing bridge in Japan [5], the Yi Sun-Sin bridge in Korea [6], the Xihoumen bridge [7–9] and the Humen bridge [10] in China. People have known that in most cases, the VIV is not catastrophic and does not damage bridge components or threaten structural safety. However, excessive vibration may cause driver discomfort and interrupt bridge operations [11]. For example, the

Humen bridge was forced to close for 10 days [12]. Therefore, VIV is a major concern for bridge maintenance, and the mathematical modeling of bridge VIV is a long-term research topic in wind engineering [13].

Initially, the classical VIV models of bluffs have been adopted for the slender structures [14]. When the flow passes through an elastically mounted bluff body, the vortices are generated in the body wake [15]. The frequency of vortex shedding is normally proportional to the flow velocity, which is characterized by a dimensionless Strouhal number St defined as fD/U [16] (f is the dominant frequency of vortex shedding; D is a characteristic dimension of the bluff-body; U is the mean incident flow velocity). When the vortex-shedding frequency matches with the bluff-body fundamental vibration frequency, resonance occurs between the bluff-body and vortices. As wind speeds increase, this resonance continues as the vortex frequency is captured by the vibration frequency. This phenomenon is called frequency lock-in [16]. During the VIV lock-in range, the bluff body is self-excited and also self-limited. For certain bluff body shapes, such as the circular cylinder, the hysteresis effect is observed [17]. As wind speeds increase beyond the lock-in range, both the resonance and the VIV disappear.

1.2 Recent challenges in the VIV modeling for long-span bridge

In order to mathematically investigate the VIV response, several semi-empirical models were developed. The first intuitive mode is the wake-oscillator model. The wake vortex is modeled as a self-exciting and self-limiting oscillator, which interacts with the bluff body dynamically [18]. On the other hand, the single degree-of-freedom model (SDOF) was also widely used in wind engineering because of its simplicity, which uses a single ordinary differential equation to describe the vibration behavior of the bluff body [14]. The most famous SDOF model is Scanlan's nonlinear VIV model [19], which uses frequency-dependent aerodynamic damping and stiffness (flutter derivatives) and a quadratic term to modify aerodynamic damping; thus, this model is equivalent to the van der Pol oscillator [20]. In addition to these semi-empirical models, an unstable and nonlinear model is proposed in [21] to consider the limit cycle oscillation (LCO), frequency shift, hysteresis, and beat phenomenon.

In recent years, as an increasing number of VIVs occurs on several long-span bridges, the simple mathematical format of the SDOF model has attracted the attention of scholars, and several other VIV models have been developed, such as the Rayleigh oscillator model [22]. The performance of the different VIV models was compared [23]. The calibration of the VIV model coefficients is also important in engineering applications. Professor Tamura suggested that the coefficients should be derived based on a physical interpretation [17]. However, it is also difficult to derive all coefficients when the bridge geometry system becomes complex. Therefore, many coefficients regression methods, such as direct aerodynamic measurements [24] and curve fitting through instantaneous aerodynamic damping and stiffness [23,25], have also been developed.

Due to the mutual frequency locking of bluff bodies and vortices, only one dynamic mode can be excited during VIV. Therefore, most mathematical models focus on a single structural mode that is potentially vulnerable to VIV. However, for long-span bridges with multiple closely spaced modes due to extreme flexibility, there are several modes that are potential to be excited. Field measurements of bridge VIV have yielded contradictory results. For example, Xihoumen Bridge (1650 m span) has been affected by VIV for more than 10 years, and four VIV modes are frequently observed in Fig. 1a. The VIV lock-in ranges for different modes are largely overlapping, indicating that there is more than one VIV mode for a certain wind speed. On the contrary, only one VIV mode (0.233 Hz) has been observed on Humen Bridge (888 m span), and the other potential VIV modes (0.277 Hz) also have an overlap lock-in range, but this VIV mode has not been recorded [26].

On the other side, several important technologies had been developed in recent year to improve the solution accuracy and efficiency, such as Bilinear residual network method [27], bilinear neural network method [28–30] and symbol calculation method based on neural network [31–34]. Other nonlinear dynamic physical and mathematical problems, such as oceanic wave in the shallow water [35–40], liquid and lattice [41], blood circulatory system [42], electrical lattice [43] and optical medium [44], have also developed many novel methods, which are beneficial for nonlinear vortex-induced vibration analysis.
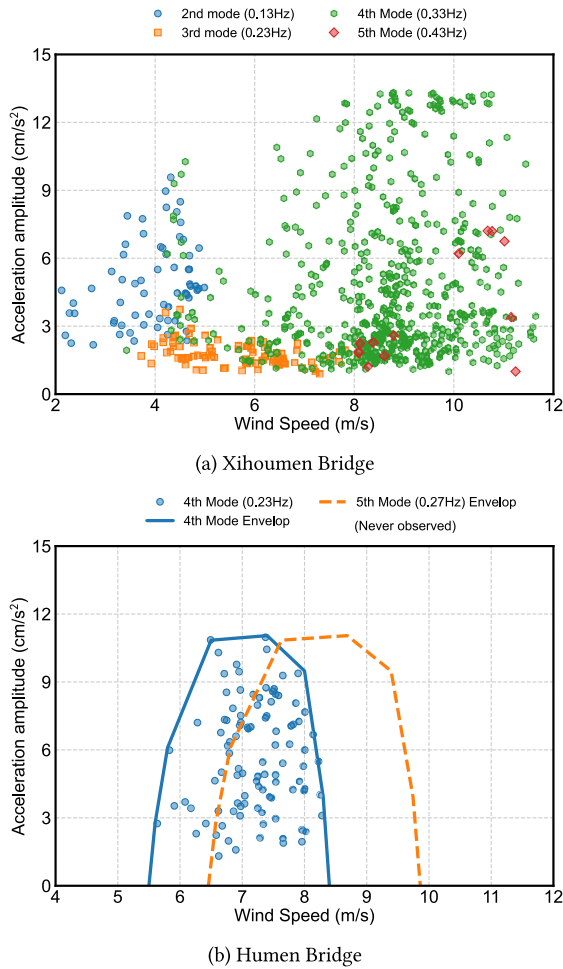
(a) Xihoumen Bridge

(b) Humen Bridge

Fig. 1 Excited modes of long-span bridges during VIV

1.3 Main motivation and objectives

Because of the above mentioned phenomenon, the traditional single DOF model is not suitable for long-span bridges with multiple closely spaced modes. Considering that VIV is a classical nonlinear dynamic process [45], the multiple modes are coupled together since the classical linear dynamic decomposition cannot be applied. This paper proposes an analytical method to study the mode coupling effect of long-span bridges during VIV considering multiple closely spaced modes. The amplitudes evolution during multimode VIV are derived based on averaging method. From the proposed method, the mode competition phenomenon is discovered. For the bridge VIV with multiple modes, there is always one mode that evolves while

the other mode decays. The final stable VIV mode depends on the initial condition of VIV.

2 Theoretical analysis of bridge deck VIV

2.1 Mathematical modelling of VIV

At the arbitrary location x along the bridge deck with span as L, the governing motion equation for nonlinear VIV is

$$M(x)\frac{d^2z(x)}{dt^2} + C(x)\frac{dz(x)}{dt} + K(x)z(x)$$
$$= \rho U^2 D \left[\left(Y_1 - h\left(\frac{z(x)}{D}\right) \right) \frac{\frac{dz(x)}{dt}}{U} + Y_2 \frac{z(x)}{D} \right],$$
(1)

where $z(x)$ is the vibration amplitude of bridge deck at location x, M-C-K are the structural mass, damping and stiffness, respectively. ρ is the air density and Y_1, Y_2 are linear aeroelastic damping, linear aeroelastic stiffness depending on the vibration frequency.

If, at certain wind speeds, there are two potential modes excited by vortex-induced effect, the vibration can be considered as the superposition of two modes (double degrees of freedom, DDOF) as in

$$z(x) = \phi_1(x)y_1 + \phi_2(x)y_2 = \begin{bmatrix} \phi_1(x) & \phi_2(x) \end{bmatrix} \begin{bmatrix} y_1 \\ y_2 \end{bmatrix}.$$
(2)

The situation in which the VIV lock-in region contains more than two modes with the same wind speed is extremely rare, which will not be considered.

Then the governing equation becomes as

$$\begin{bmatrix} m_1 & \\ & m_2 \end{bmatrix} \begin{bmatrix} \frac{d^2y_1}{dt^2} \\ \frac{d^2y_2}{dt^2} \end{bmatrix} + \begin{bmatrix} 2m_1\omega_1\xi_1 & \\ & 2m_2\omega_2\xi_2 \end{bmatrix} \begin{bmatrix} \frac{dy_1}{dt} \\ \frac{dy_2}{dt} \end{bmatrix}$$
$$+ \begin{bmatrix} m_1\omega_1^2 & \\ & m_2\omega_2^2 \end{bmatrix} \begin{bmatrix} y_1 \\ y_2 \end{bmatrix} = \boldsymbol{\phi}^2 \rho U^2 DL\boldsymbol{Y}_1 \begin{bmatrix} \frac{dy_1}{dt} \\ \frac{dy_2}{dt} \end{bmatrix} / U$$
$$+ \boldsymbol{\phi}^2 \rho U^2 DL\boldsymbol{Y}_2 \begin{bmatrix} y_1 \\ y_2 \end{bmatrix} / D$$
$$- \boldsymbol{\phi}^2 \rho U^2 DL\boldsymbol{h} \left(\frac{\phi_1(x)y_1 + \phi_2(x)y_2}{D} \right) \begin{bmatrix} \frac{dy_1}{dt} \\ \frac{dy_2}{dt} \end{bmatrix} / U,$$
(3)

in which

$$\boldsymbol{\phi}^2 = \int_0^1 \begin{bmatrix} \phi_1(x/L) \\ \phi_2(x/L) \end{bmatrix} [\phi_1(x/L)\ \phi_2(x/L)]\, dx$$
$$= \begin{bmatrix} \phi_{11} & 0 \\ 0 & \phi_{22} \end{bmatrix}$$

and $\phi_{12} = 0$ because of modal shape orthogonality, m_1, ξ_1, ω_1 are modal mass, damping coefficient and frequency for first mode and m_2, ξ_2, ω_2 are similar quantities for second mode. For the nonlinear aeroelastic function, the modal shape integral will be included in $\boldsymbol{h}()$, which will be explicitly discussed later. $\boldsymbol{Y}_1, \boldsymbol{Y}_2$ are linear aeroelastic damping, linear aeroelastic stiffness depending on the vibration frequency ω_1 and ω_2 of the corresponding mode. $\boldsymbol{h}()$ is nonlinear aeroelastic damping function $\boldsymbol{h}() = \mathrm{diag}\,[h_1()\ h_2()]$.

Next, non-dimensional motion is defined as $\eta = y/D$, K is the reduced frequency $K = \omega \dfrac{D}{U}$, and $\dot{\eta}$ indicates the differentiation of η with respect to dimensionless time $\tau = U\dfrac{t}{D}$. The governing equation in dimensionless form is

$$[\ddot{\eta}_1 \ddot{\eta}_2] + [2K_1\xi_1\ \ \& 2K_2\xi_2][\dot{\eta}_1 \dot{\eta}_2]$$
$$+ [K_1^2\ \ \& K_2^2][\eta_1 \eta_2] = \boldsymbol{\phi}^2 \boldsymbol{m}^* \boldsymbol{Y}_1 [\dot{\eta}_1 \dot{\eta}_2] \tag{4}$$
$$- \boldsymbol{\phi}^2 \boldsymbol{m}^* \boldsymbol{h}(\eta_1, \eta_2) \begin{bmatrix} \dot{\eta}_1 \\ \dot{\eta}_2 \end{bmatrix} + \boldsymbol{\phi}^2 \boldsymbol{m}^* \boldsymbol{Y}_2 \begin{bmatrix} \eta_1 \\ & \eta_2 \end{bmatrix},$$

where $\boldsymbol{m}^*$ is the mass ratio matrix $\boldsymbol{m}^* = \rho D^2 L \begin{bmatrix} m_1 \\ & m_2 \end{bmatrix}^{-1}$.

The above equation can be rewritten in compact matrix format,

$$\ddot{\boldsymbol{\eta}} + [\boldsymbol{\epsilon} + \boldsymbol{g}(\boldsymbol{\eta})]\dot{\boldsymbol{\eta}} + \boldsymbol{\kappa}^2 \boldsymbol{\eta} = 0, \tag{5}$$

where $\boldsymbol{\eta} = \begin{bmatrix} \eta_1 \\ \eta_2 \end{bmatrix}$, $\boldsymbol{\epsilon} = \begin{bmatrix} 2K_1\xi_1 & \\ & 2K_2\xi_2 \end{bmatrix} - \boldsymbol{\phi}^2 \boldsymbol{m}^* \boldsymbol{Y}_1$, $\boldsymbol{g}(\boldsymbol{\eta}) = \boldsymbol{\phi}^2 \boldsymbol{m}^* \boldsymbol{h}(\eta_1, \eta_2)$.

Supposing the solutions to Eq. (5) are harmonic with small perturbation as:

$$\eta_1 = A_1 \cos(\kappa_1 \tau + \psi_1) + o(\epsilon_1) \tag{6a}$$
$$\dot{\eta}_1 = -\kappa_1 A_1 \sin(\kappa_1 \tau + \psi_1) + o(\epsilon_1) \tag{6b}$$
$$\eta_2 = A_2 \cos(\kappa_2 \tau + \psi_2) + o(\epsilon_2) \tag{6c}$$
$$\dot{\eta}_2 = -\kappa_2 A_2 \sin(\kappa_1 \tau + \psi_2) + o(\epsilon_2), \tag{6d}$$

in which κ_1 are the angular frequency of the solutions to be determined.

Next, the total energy of mode 1 is

$$E_1 = \frac{1}{2}\kappa_1 \eta_1^2 + \frac{1}{2}\dot{\eta}_1^2. \tag{7}$$

On the other hand, when the vibration reaches maximum amplitudes, the total energy is

$$E_1 = \frac{1}{2}\kappa_1 A_1^2. \tag{8}$$

Dividing the above formulas by κ_1 and differentiate of it,

$$\frac{1}{2}A_1^2 = \frac{1}{2}\eta_1^2 + \frac{1}{2}\frac{\dot{\eta}_1^2}{\kappa_1} + o(\epsilon_1^2)$$
$$\Rightarrow A_1 \dot{A}_1 = \eta_1 \dot{\eta}_1 + \frac{\dot{\eta}_1 \ddot{\eta}_1}{\kappa_1^2} = \eta_1 \dot{\eta}_1$$
$$+ \frac{\dot{\eta}_1 \left[-\kappa_1^2 \eta_1 - \epsilon_1 \dot{\eta}_1 - g_1(\eta_1, \eta_2)\dot{\eta}_1\right]}{\kappa_1}$$
$$= \frac{-\epsilon_1 \dot{\eta}_1^2 - g_1(\eta_1, \eta_2)\dot{\eta}_1^2}{\kappa_1} \tag{9}$$
$$= \frac{[-\epsilon_1 - g_1(\eta_1, \eta_2)]\dot{\eta}_1^2}{\kappa_1}$$
$$= A_1^2 \kappa_1 \sin^2(\kappa_1 \tau + \psi_1)[-\epsilon_1 - g_1(\eta_1, \eta_2)]$$
$$\Rightarrow \dot{A}_1 = -A_1 \kappa_1 \sin^2(\kappa_1 \tau + \psi_1)[\epsilon_1 + g_1(\eta_1, \eta_2)].$$

Similarity, the differentiation of the amplitude of mode 2

$$\dot{A}_2 = -A_2 \kappa_2 \sin^2(\kappa_2 \tau + \psi_2)[\epsilon_2 + g_2(\eta_1, \eta_2)], \tag{10}$$

where $g_1(\eta_1, \eta_2) = \phi_{11} m_1^* h(\eta_1, \eta_2)$ and $g_2(\eta_1, \eta_2) = \phi_{22} m_2^* h(\eta_1, \eta_2)$

2.2 Coupled two modes VIV amplitudes evolution function

For the VIV dynamics system with two modes, the aeroelastic parameters are depending on the reduced frequency. Taking the nonlinear function $h()$ for mode 1 as example,

$$g_1(\eta_1, \eta_2) = m_1^* \sum_{i=1}^{N} a_i(\kappa_1) \int_0^1 \phi_1^2 [\phi_1\left(\frac{x}{L}\right)\eta_1$$
$$+ \phi_2\left(\frac{x}{L}\right)\eta_2]^i\, dx$$
$$= m_1^* \sum_{i=1}^{N} a_i(\kappa_1) \sum_{j=0}^{i} \binom{i}{j} \int_0^1 \phi_1^2$$
$$\left(\frac{x}{L}\right)\left[\phi_1\left(\frac{x}{L}\right)\eta_1\right]^j \left[\phi_2\left(\frac{x}{L}\right)\eta_2\right]^{i-j}\, dx$$

$$=m_1^* \sum_{i=1}^{N} a_i(\kappa_1) \sum_{j=0}^{i} \binom{i}{j} \phi_1^{j+2}$$
$$\otimes \phi_2^{ij} \, eta_1^j \eta_2^{i-j}, \tag{11}$$

where the extra ϕ_1^2 is from the modal shape effect in Eq. (3), and $\phi_1^{j+2} \otimes \phi_2^{i-j} = \int_0^1 \left[\phi_1\left(\frac{x}{L}\right)\right]^{j+2} \left[\phi_2\left(\frac{x}{L}\right)\right]^{i-j} dx$

However, not all components in the above formula are necessary, because, on one sides, odd i does not contribute to the vibration energy, and, on the other sides, odd j is omitted since the modal shape orthogonality, such as $\phi_1^3 \otimes \phi_2^1 = 0$ ($i = 2$, $j = 1$). Then the above formulas is reduced as:

$$g_1(\eta_1, \eta_2) = m_1^* \sum_{i=1}^{N/2} a_{2i}(\kappa_1) \sum_{j=0}^{i} \binom{2i}{2j}$$
$$\phi_1^{2j+2} \otimes \phi_2^{2i-2j} \eta_1^{2j} \eta_2^{2i-2j}. \tag{12}$$

Similarly, the nonlinear aeroelastic function for mode 2 is:

$$g_2(\eta_1, \eta_2) = m_2^* \sum_{i=1}^{N/2} a_{2i}(\kappa_2) \sum_{j=0}^{i} \binom{2i}{2j}$$
$$\phi_1^{2j} \otimes \phi_2^{2i-2j+2} \eta_1^{2j} \eta_2^{2i-2j}. \tag{13}$$

Next, the amplitude evolution function for mode 1 is

$$\dot{A}_1 = -A_1\kappa_1 \sin^2(\kappa_1\tau + \psi_1) \left\{ \epsilon_1(\kappa_1) + m_1^* \sum_{i=1}^{N/2} a_{2i}(\kappa_1) \right.$$
$$\left. \sum_{j=0}^{i} \binom{2i}{2j} \phi_1^{2j+2} \otimes \phi_2^{2i-2j} \eta_1^{2j} \eta_2^{2i-2j} \right\}$$
$$= -A_1\kappa_1 \sin^2(\kappa_1\tau + \psi_1) \left\{ \epsilon_1(\kappa_1) + m_1^* \right.$$
$$\sum_{i=1}^{N/2} a_{2i}(\kappa_1) \sum_{j=0}^{i} \binom{2i}{2j} \phi_1^{2j+2} \otimes \phi_2^{2i-2j}$$
$$\left. [A_1 \cos(\kappa_1\tau + \psi_1)]^{2j} [A_2 \cos(\kappa_1\tau + \psi_2)]^{2i-2j} \right\}$$
$$= -A_1\kappa_1 \sin^2(\kappa_1\tau + \psi_1) \left\{ \epsilon_1(\kappa_1) + m_1^* \right.$$
$$\sum_{i=1}^{N/2} a_{2i}(\kappa_1) \cos^{2i}(\kappa_1\tau + \psi_1)$$

$$\left. \sum_{j=0}^{i} \binom{2i}{2j} \phi_1^{2j+2} \otimes \phi_2^{2i-2j} A_1^{2j} A_2^{2i-2j} \right\}. \tag{14}$$

Then, the averging methods is applied to the above formula again

$$\dot{A}_1 = -A_1\kappa_1 \left\{ \epsilon_1(\kappa_1)I_0 + m_1^* \sum_{i=1}^{N/2} a_{2i}(\kappa_1) I_{2i} \sum_{j=0}^{i} \binom{2i}{2j} \right.$$
$$\left. \phi_1^{2j+2} \otimes \phi_2^{2i-2j} A_1^{2j} A_2^{2i-2j} \right\}. \tag{15}$$

Similarly, for mode 2, the amplitude evolution function is:

$$\dot{A}_2 = -A_2\kappa_2 \left\{ \epsilon_2(\kappa_2)I_0 + m_2^* \sum_{i=1}^{N/2} a_{2i}(\kappa_2) I_{2i} \sum_{j=0}^{i} \binom{2i}{2j} \right.$$
$$\left. \phi_1^{2j} \otimes \phi_2^{2i-2j+2} A_1^{2j} A_2^{2i-2j} \right\}, \tag{16}$$

where $I_0 = \frac{1}{2\pi} \int_{-\pi}^{\pi} \sin^2(T + \phi) dT = \frac{1}{2}$ and $I_{2i} = \frac{1}{2\pi} \int_{-\pi}^{\pi} \sin^2(T + \phi) \cos^{2i}(T + \phi) dT = \frac{2i-1}{2i+2} I_{2i-2}$.

The equilibrium points are the roots for the following coupled bi-variables higher order polynomials

$$-A_1\kappa_1 \left\{ \epsilon_1(\kappa_1)I_0 + m_1^* \sum_{i=1}^{N/2} a_{2i}(\kappa_1) I_{2i} \sum_{j=0}^{i} \binom{2i}{2j} \right.$$
$$\left. \phi_1^{2j+2} \otimes \phi_2^{2i-2j} A_1^{2j} A_2^{2i-2j} \right\} = 0 \tag{17a}$$

$$-A_2\kappa_2 \left\{ \epsilon_2(\kappa_2)I_0 + m_2^* \sum_{i=1}^{N/2} a_{2i}(\kappa_2) I_{2i} \sum_{j=0}^{i} \binom{2i}{2j} \right.$$
$$\left. \phi_1^{2j} \otimes \phi_2^{2i-2j+2} A_1^{2j} A_2^{2i-2j} \right\} = 0. \tag{17b}$$

2.3 VIV parameters determination method from SDOF sectional model tests

Since it it difficult to directly evaluate the aeroelastic parameters of VIV on the full scale bridge, sectional model tests were conducted to examine the VIV response and determine the aeroelastic parameters, including Y_1, Y_2 and the nonlinear aeroelastic force function $h()$. For the sectional model operated in wind

tunnel, the above equation is reduced to 1 mode with $\phi_1 = 1$, thus the governing equation is

$$\ddot{\eta} + 2K\xi\dot{\eta} + K^2\eta = m^*Y_1\dot{\eta} - m^*h(\eta)\dot{\eta} + m^*Y_2\eta. \tag{18}$$

The amplitude evolution rate is

$$\dot{A} = -A\kappa \sin^2(\kappa\tau + \psi)[\epsilon + g(\eta)]. \tag{19}$$

Obviously, $\kappa = \sqrt{K^2 - m^*Y_2}$ for SDOF system.

As in the simpler case, the VIV stability analysis for a sectional model with single DOF will be discussed first. If the nonlinear aeroelastic force is expanded into Taylor series as:

$$g(\eta) = \sum_{i=1}^{N} b_i \eta^i \quad h(\eta) = \sum_{i=1}^{N} a_i \eta^i, \tag{20}$$

where $b_i = a_i * m_1$. Next, the amplitude evolution function became as

$$\dot{A} = -A\kappa \sin^2(\kappa\tau + \phi)[\epsilon + g(\eta)]$$
$$= A\kappa \sin^2(\kappa\tau + \phi)\left[\epsilon + \sum_{i=1}^{N} b_i A^i \cos^i(\kappa\tau + \phi)\right]. \tag{21}$$

Because Eq. (18) is a weakly nonlinear damped dynamic system, the amplitude evolution varies much slowly and can be considered as constant during one vibration cycle. Therefore, the averaged amplitude evolution during one cycle is considered as constant as

$$\dot{A} = \frac{1}{2\pi} A\kappa \int_{-\pi}^{\pi} \sin^2(T + \phi)$$
$$\left[\epsilon + \sum_{i=1}^{N} b_i A^i \cos^i(T + \phi)\right] dT$$
$$= \frac{A\kappa}{2\pi}\left[\epsilon \int_{-\pi}^{\pi} \sin^2(T + \phi) dT\right.$$
$$\left. + \sum_{i=1}^{N} b_i A^i \int_{-\pi}^{\pi} \sin^2(T + \phi)\cos^i(T + \phi) dT\right]. \tag{22}$$

When i is odd, the above integral in one period is 0, and only the terms with even i are kept in the above formula. The differentiation of vibration amplitude is rewritten as

$$\dot{A} = -A\kappa\left[\epsilon I_0 + \sum_{i=1}^{N/2} b_{2i} I_{2i} A^{2i}\right]. \tag{23}$$

From Eq. (23), the equilibrium points can be found when $\epsilon I_0 + \sum_{i=1}^{N/2} b_{2i} I_{2i} A_1^{2i} = 0$. If VIV enters a limit-cycle oscillation (LCO), there must be one stable equilibrium point at the VIV LCO amplitude. There will
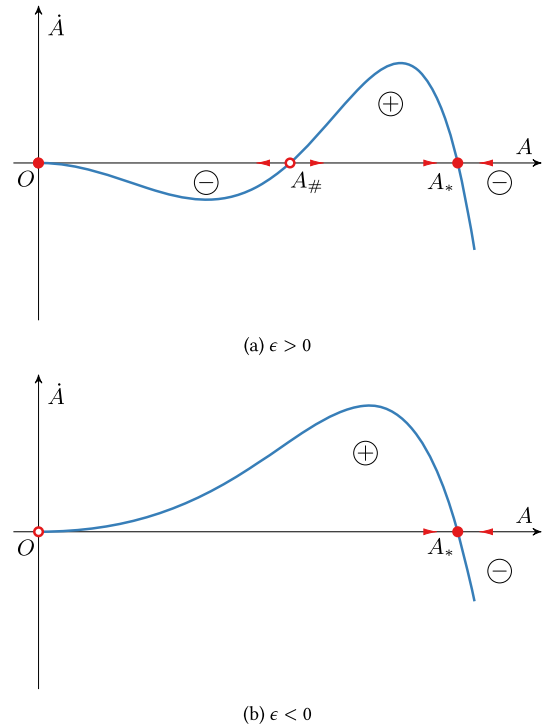

(a) $\epsilon > 0$

(b) $\epsilon < 0$

Fig. 2 Stability of equilibrium points for single DOF VIV (legends: ○, unstable equilibrium point; ●, stable equilibrium point; ⊖, energy decays; ⊕, energy gains;)

be two scenarios: one is $\epsilon > 0$ (the structural damping is larger than the linear part of the aeroelastic damping) and the other is $\epsilon < 0$ (the structural damping is smaller than the linear part of the aeroelastic damping). For $\epsilon < 0$ in Fig. 2b, the $\dot{A}_1$ is always positive until the VIV amplitude reaches the stable equilibrium point. This case is equivalent to the traditional Scanlan VIV model [19]. However, for $\epsilon > 0$ in Fig. 2a, there will be an unstable equilibrium point before the VIV LCO amplitude, which means that the structural amplitude must exceed this unstable equilibrium point to excite the vortex force and then reach the VIV LCO amplitude. If the structural amplitude is smaller than the unstable equilibrium point, it will return to the zero amplitude.

2.4 Stability analysis of equilibrium points

At the equilibrium points, $\dot{A}_1 = 0$ and $\dot{A}_2 = 0$. However, the dynamics system may be stable or unstable. When the system is stable, the dynamics system still converges to equilibrium points after a small perturba-
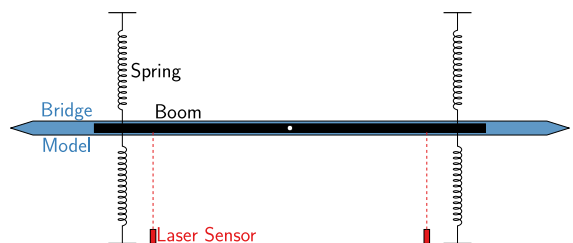
tion. When the system is unstable, the dynamics system will move away from the equilibrium points after a small perturbation. Taking the unstable equilibrium points ($A_\#$ and A_*) in Fig. 2a as an example, $\dot{A} < 0$ for $A \to A_\#^-$ and $\dot{A} < 0$ for $A \to A_\#^+$, therefore $A_\#$ is an unstable equilibrium point. On the other hand, $\dot{A} > 0$ for $A \to A_*^-$ and $\dot{A} < 0$ for $A \to A_*^+$, so A_* is a stable equilibrium point. In other words, the necessary condition for stability is $d\dot{A}/dA < 0$, and similarly $d\dot{A}/dA > 0$ indicates unstable equilibrium points.

It is easy to extend the above stability analysis methods to the equilibrium points ($\dot{A}_1 = 0$, $\dot{A}_2 = 0$) of double degrees of freedom. For the stable equilibrium point ($d\dot{A}_1/dA_1 < 0$, $d\dot{A}_2/dA_2 < 0$); while for the unstable equilibrium point, ($d\dot{A}_1/dA_1 > 0$, $d\dot{A}_2/dA_2 > 0$). Both ($d\dot{A}_1/dA_1 > 0$, $d\dot{A}_2/dA_2 < 0$) and ($d\dot{A}_1/dA_1 < 0$, $d\dot{A}_2/dA_2 > 0$) are saddle points, which means stable for one DOF but unstable for another DOF. The stability of equilibrium points will be further illustrated with an application example.

3 VIV parameters determination from wind tunnel test

3.1 Experimental setup

The wind tunnel test was carried out in the TJ-1 wind tunnel of Tongji University, which is a closed-circuit wind tunnel with a test section that is 1.8 m wide and 1.8 m high. The operational airflow velocity is 1-15 m/s.

Humen Bridge, which is a suspension bridge with 888 m main span, is used as the prototype in this study. The elevation of the Humen Bridge is plotted in Fig. 3. This bridge girder is a standard streamlined closed-box section. The length scale of the sectional model is 50:1 to ensure that the wind tunnel blockage ratio is less than 1%. Detailed geometry information is plotted in Fig. 4b, and the view of the sectional model in the TJ-2 wind tunnel is shown in Fig. 4a.

(a) Sectional model in the TJ-1 wind tunnel

(b) Geometry of Sectional model (left: model scale units: mm, right: full scale, units: m; geometries of accessory components can be found in [11])

Fig. 4 Bridge deck sectional model tested in wind tunnel

Fig. 5 Schematic plot of the suspended sectional model

The width, height and length of the sectional model are 712 mm, 53.4 mm, and 1740 mm, respectively. The traditional suspension system is used to simulate the vibration of the bridge deck. Four laser displacement sensors are placed at two ends of the suspension boom to measure the wind-induced vibration signal of the bridge section during VIVs. The layout of the bridge deck suspension system is plotted in Fig. 5.
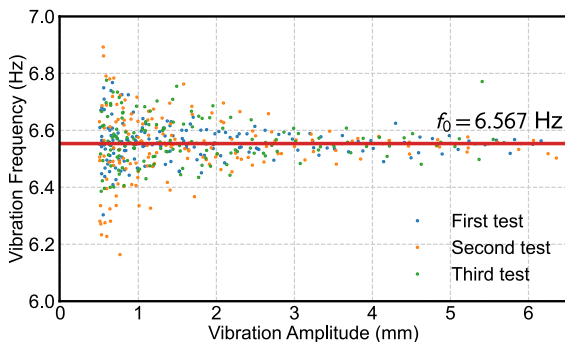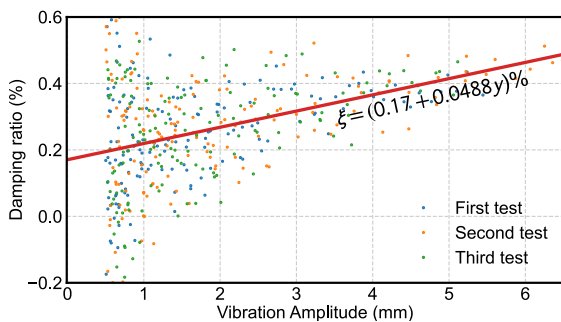
Fig. 6 Vibration frequency at different amplitude

Fig. 7 Damping ratios at different amplitude

3.2 Dynamic characters identification

The total mass including the model, the booms and the springs (elongated part) is 16.4 kg, the vertical vibration frequency f_0 and the damping ratios ξ of the suspension system were identified by free decay vibration tests. The relationship between instantaneous dynamic characters and vibration amplitudes (damping ratio and frequency), which are extracted from the Hilbert transformation [46], is plotted in Figs. 6 and 7. The vibration frequency remains stable at different amplitudes in Fig. 6. On the contrary, the damping ratios increase with the amplitudes. As shown in Fig. 7, the damping ratios of the suspension system vary almost linearly with the amplitudes, the quadratic term. Because only vertical VIVs are considered, rotational inertia and frequency are not reported in this study.

3.3 Aeroelastic parameters identification during VIV

The standard VIV test is performed on the bridge section model and VIV is observed when the reduced wind speeds $V = U/Df_0$ are within the range (9.8, 13.2) and
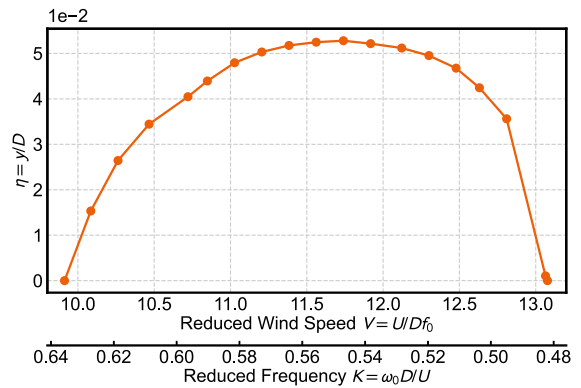
Fig. 8 VIV lock-in region from wind tunnel tests
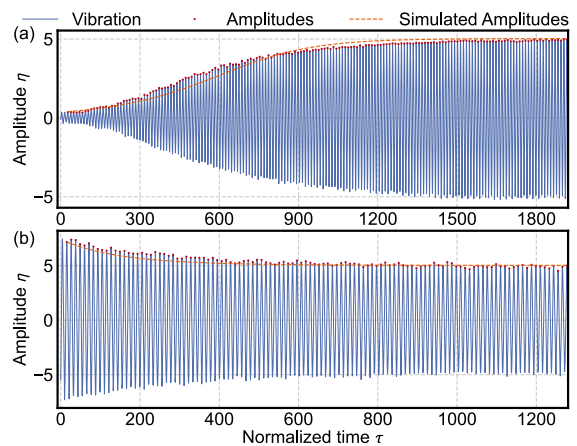
Fig. 9 VIV parameters identification based on amplitudes evolution ($K = 0.5614$, $V = 11.19$, a:grow to resonance b:decay to resonance)

the corresponding reduced frequency is (0.476, 0.641). In the VIV lock-in region, the stable amplitudes of the VIV are examined by increasing the wind speeds, and the reduced wind speed interval is around $\Delta V = 0.178$. The dimensionless amplitudes within lock-in region is plotted in Fig. 8. In addition to increasing wind speeds, VIV tests are also performed by decreasing wind speeds. However, the VIV amplitudes are exactly the same between two testing scenarios of increasing and decreasing wind speeds. Therefore, the VIV hysteresis phenomenon is not observed for this bridge section.

After examining the VIV amplitudes, the grow-to-resonance test is performed at each wind speed. The bridge model is released near the 0 amplitude location; the vortex-induced force will excite the model until reaching the stable vibration amplitudes. Fig-
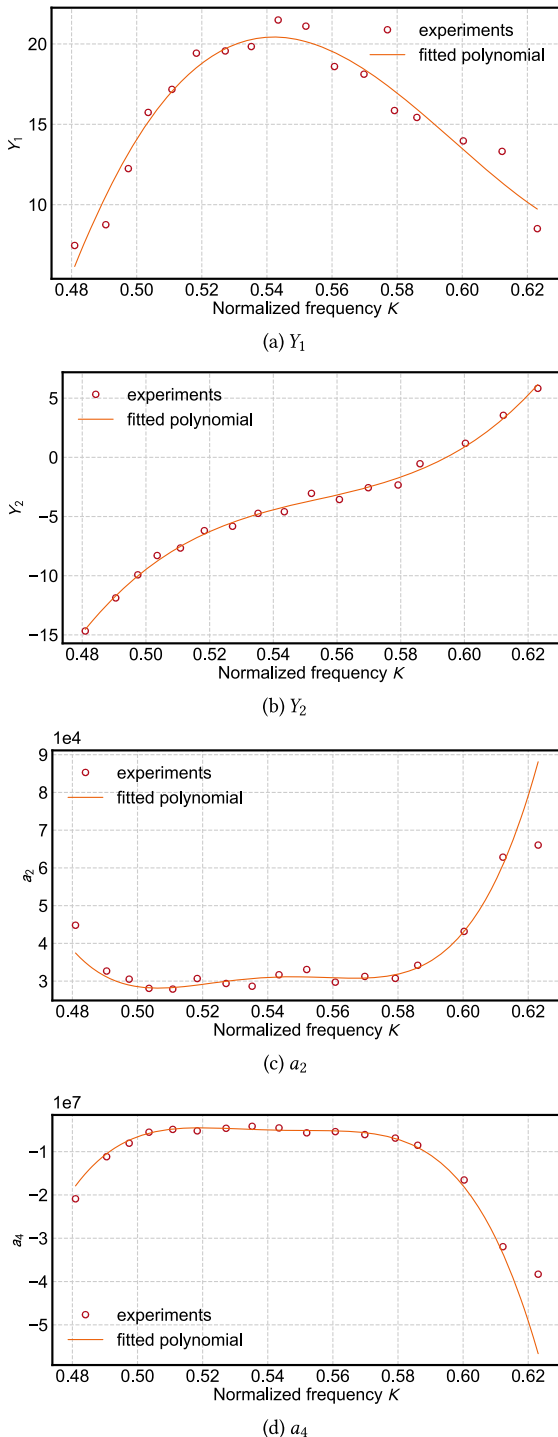
(a) Y_1

(b) Y_2

(c) a_2

(d) a_4

Fig. 10 Identified aeroelastic parameters from VIV amplitudes evolution
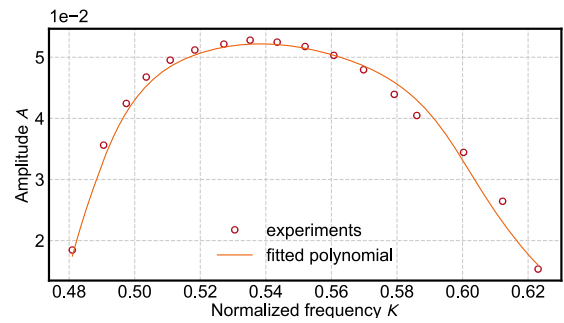

Fig. 11 VIV comparison between wind tunnel tests and fitted polynomials of aeroelastic parameters

ure 9a shows the grow-to-resonance vibration records at dimensionless scale, and during each vibration cycle, the maximum response is identified as the amplitudes. Next, the identification of VIV aeroelastic parameters based on constrained optimization is performed on the amplitude evolution process, and the constraint is applied to ensure that the stable amplitudes match the experimental results. Using the identified parameters, the evolution of the amplitude $A(\tau)$ can be numerically simulated using Eq. (23). The polynomial expansion order N is also examined, the results show that $N = 4$ is sufficient to simulate the nonlinear aerodynamic during the VIV. Furthermore, the decay-to-resonance tests was also carried out at each wind speed. The identified parameters from grow-to-resonance are used to simulate amplitude evolution $A(\tau)$ of decay-to-resonance as displaced in Fig. 9b. The simulated evolution of the amplitude $A(\tau)$ is very identical to the experimental results, demonstrating that the identified aeroelastic parameters can well capture the nonlinear dynamic characters from 0 to the stable vibration, and also have the extrapolation ability when vibration exceeds the stable amplitudes, because the decay-to-resonance process is not involved in the identification of parameters.

Through repeating the above parameter identification for each wind speeds, the aeroelastic parameters for the wind speeds within lock-in region are illustrated in Fig. 10. The linear part of the aeroelastic damping parameter Y_1 as shown in Fig. 10a has trends similar to the VIV amplitudes, which means that when the VIV amplitudes are large, the linear aeroelastic damping Y_1 is also large. The aeroelastic stiffness parameter Y_2 is positively correlated with reduced frequency (negatively correlated with wind speeds). The nonlinear aeroelastic parameters a_2 and a_4 are plotted in Figs. 10c

Table 1 Structural dynamic mode characters

	Frequency (Hz)	Modal mass (kg/m)	Modal shape function
Mode 1	0.233	20819	$0.36 - 0.574\cos(0.0126x/L)$
Mode 2	0.277	20931	$-0.99\sin(0.0142x/L)$
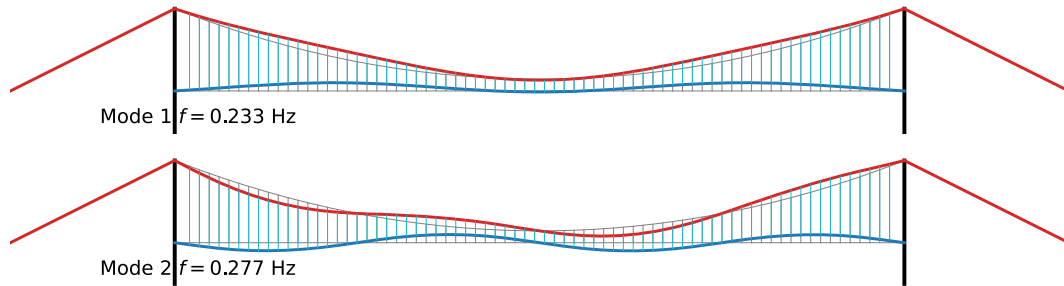
Fig. 12 Two close mode shapes of Humen Bridge

and 10d. a_2 is positive and a_4 is negative, and they have different varying trends with reduced frequency. In order to smooth out the identified aeroelastic parameters, polynomials are employed to fit the experimental results. The polynomial expansion orders for Y_1, Y_2, a_2 and a_4 are 2, 3, 4 and 4, respectively. The fitted polynomial of aeroelastic parameters is also plotted in Fig. 10.

Based on the smoothed aeroelastic parameter functions $Y_1(K)$, $Y_2(K)$, $a_2(K)$ and $a_4(K)$, the stable amplitudes for different wind speeds can be calculated based on Eq. (23). Figure 11 shows the calculated amplitudes from fitted functions $Y_1(K)$, $Y_2(K)$, $a_2(K)$, and $a_4(K)$ compared with wind tunnel tests, demonstrating that the fitted function can well present VIV parameters within the lock-in region.

4 VIV two modes competition mechanism

After the determination of VIV aeroelastic parameters, the evolution rates of the amplitudes of two modes can be evaluated at different amplitudes.

The structural dynamics parameters, including the frequency and modal mass of the Humen bridge, are listed in Table 1. The normalized modal shapes expressed in sinusoidal functions are also shown in Table 1 and plotted in Fig. 12. It is clearly that the shape of mode 1 is symmetric and that of mode 2 is antisymmetric.

Substituting the structural parameters and aerodynamic parameters in Fig. 10 into Eqs. (15) and (16), the evolution rate of VIV amplitudes in two modes $(\dot{A}_1, \dot{A}_2)$ can be evaluated at different combinations of amplitudes. The evolutionary rates are plotted as streamline plots for different wind speeds $U = 8.4$, 8.6, 8.8 and 9.0 m/s. In Fig. 13a, there are 3 equilibrium points with different stability. The origin point $(0,0)$ is divergent at both direction $(\frac{d\dot{A}_1}{dA_1} > 0, \frac{d\dot{A}_2}{dA_2} > 0)$. The equilibrium point $(0,0.028)$ is convergent along the A_2 axis but divergent along A_1 axis $(\frac{d\dot{A}_1}{dA_1} > 0, \frac{d\dot{A}_2}{dA_2} < 0)$, which is a saddle point. Both $(0,0)$ and $(0,0.028)$ are unstable equilibrium points. The equilibrium point $(0.081,0)$ is stable $(\frac{d\dot{A}_1}{dA_1} < 0, \frac{d\dot{A}_2}{dA_2} < 0)$ because it converges in two directions. For higher wind speeds $U = 8.6$ and 8.8 m/s, the stable equilibrium points are still on the A_1 axis with different amplitudes. However, when $U = 9.0$ m/s, the stable equilibrium point changes from the A_1 axis to the A_2 axis.

The above method can be applied to the whole VIV wind speed region for two modes. Stable and unstable equilibrium points are plotted in Fig. 15. The stable equilibrium points are depicted as solid symbols and the unstable ones as hollow symbols. Before the modes switching, the VIV amplitudes of mode 1 is similar to SDOF VIV. After the modes switching at 8.9 m/s, The
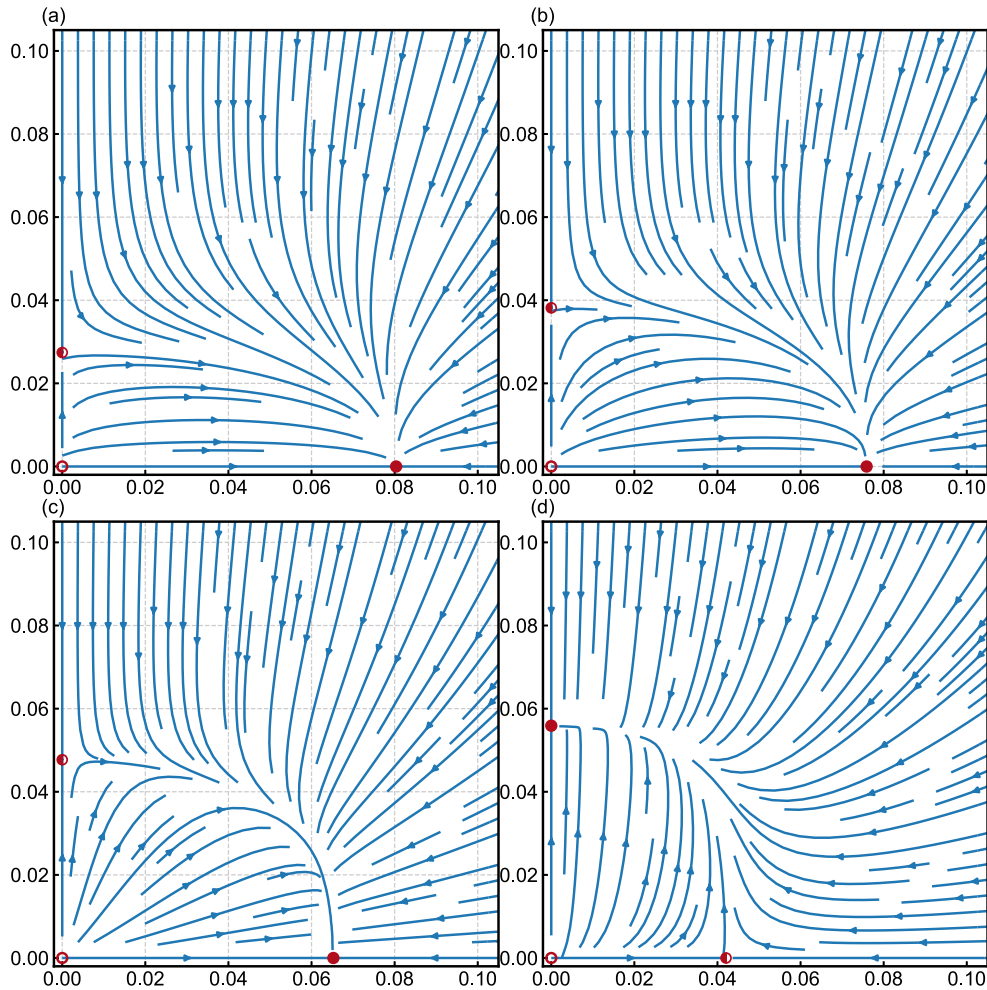
Fig. 13 The streamline plots of modes competition of VIV amplitudes (legends: ○, unstable equilibrium point; ●, point; ●, stable equilibrium point; ◑, saddle point; subplot a), $U = 8.4$ m/s; subplot b), $U = 8.6$ m/s; subplot c), $U = 8.8$ m/s; subplot d), $U = 9.0$ m/s)

VIV amplitudes are generally smaller than that of mode 1, the VIV wind speed region is wider than mode 1.

Furthermore, in order to investigate the damping effects on the two coupled modes VIV, the effective amplitudes are calculated based on Eqs. (15) and (16) with different structural damping. It is clear that the amplitudes become smaller and the VIV wind speed regions become narrower with increasing structural damping in Fig. 15. Moreover, the VIV switching wind speed slightly decreases for larger wind speeds. It should be noted that the above results are based on the analytical expansion of two-modes coupled VIV based on aerodynamic determined by traditional SDOF sec-

tional model tested in wind tunnel. In the future study, a novel sectional model vibration equipment will be developed to tested the two-modes coupled VIV in wind tunnel.

5 Conclusions

This research presents a coupled two-mode VIV model and its associated amplitude evolution equation. This model is an extension of the standard single degree-of-freedom model, which simulates the nonlinear aeroelastic force as polynomials. The nonlinear aeroelastic
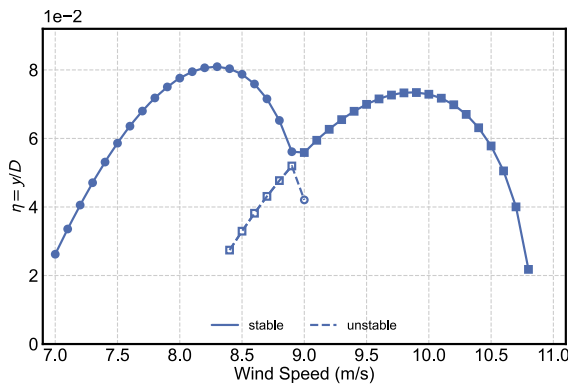
Fig. 14 The effective amplitudes from two modes for different wind speeds (O: Mode 1, □: Mode 2)
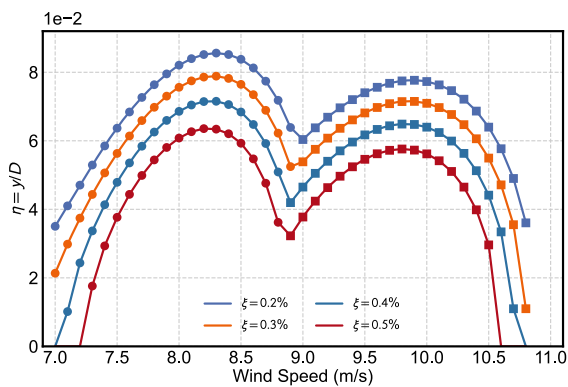

Fig. 15 The effective amplitudes for different structural damping (◯: Mode 1, ▢: Mode 2)

force causes the classical dynamic model to lose its orthogonality. The proposed VIV model takes model coupling into account as polynomials of superposition of modal displacements. After the coupled VIV dynamic model is established, the amplitude evolution equation is derived using the averaging method. The coupled two-mode VIV dynamic equation can be reduced to single mode, which can be used to identify the aeroelastic parameters for bridge sections during standard wind tunnel tests. By substituting the aeroelastic parameters into the coupled two-mode VIV amplitude evolution equation, the equilibrium points and their associated stability can be calculated. For wind speed regions with overlapping two modes VIV, there are three different stabilities: stable, unstable, and saddle points. For a given wind speed, the two modes VIV always approach the stable equilibrium point regardless of the initial condition. During the two modes coupled VIV, one mode competes with the other until

one of them is completely compressed. At lower wind speeds, the stable equilibrium point is at the mode with the lower frequency, and as the wind speed increases, the stable equilibrium point switches from the lower mode to the higher mode. Finally, the effects of structural damping on the two modes VIV are discussed. A larger structural damping ratio results in a narrower VIV wind speed region and a slightly smaller switching wind speed between modes.

Declarations

Conflict of interest The authors have no relevant financial or non-financial interests to disclose.

References

1. Zhao, L., Ge, Y.: Effects, Mechanism and Aerodynamic Mitigation of Vortex-induced Vibration of Long-span Bridges (in Chinese), 1st edn. Tongji University Pubslisher, Shanghai (2022)
2. Kumarasena, T., Scanlan, R., Ehsan, F.: Wind-induced motions of Deer Isle bridge. J. Struct. Eng. **117**(11), 3356–3374 (1991)
3. Larsen, A., Esdahl, S., Andersen, J.E., Vejrum, T.: Storebælt suspension bridge-vortex shedding excitation and mitigation by guide vanes. J. Wind Eng. Ind. Aerodyn. **88**(2–3), 283–296 (2000)
4. Frandsen, J.: Simultaneous pressures and accelerations measured full-scale on the Great Belt east suspension bridge. J. Wind Eng. Ind. Aerodyn. **89**(1), 95–129 (2001)

5. Fujino, Y., Yoshida, Y.: Wind-induced vibration and control of Trans-Tokyo Bay crossing bridge. J. Struct. Eng. **128**(8), 1012–1025 (2002)

6. Hwang, Y.C., Kim, S., Kim, H.-K.: Cause investigation of high-mode vortex-induced vibration in a long-span suspension bridge. Struct. Infrastruct. Eng. **16**(1), 84–93 (2020)

7. Li, H., Laima, S., Ou, J., Zhao, X., Zhou, W., Yu, Y., Li, N., Liu, Z.: Investigation of vortex-induced vibration of a suspension bridge with two separated steel box girders based on field measurements. Eng. Struct. **33**(6), 1894–1907 (2011)

8. Li, H., Laima, S., Zhang, Q., Li, N., Liu, Z.: Field monitoring and validation of vortex-induced vibrations of a long-span suspension bridge. J. Wind Eng. Ind. Aerodyn. **124**, 54–67 (2014)

9. Ge, Y., Yang, Y., Cao, F.: VIV sectional model testing and field measurement of xihoumen suspension bridge with twin box girder. In: Proceedings of the 13th International Conference on Wind Engineering, Amsterdam, Netherlands, pp. 11–15 (2011)

10. Zhao, L., Cui, W., Shen, X., Xu, S., Ding, Y., Ge, Y.: A fast on-site measure-analyze-suppress response to control vortex-induced-vibration of a long-span bridge. Structures **35**, 192–201 (2022)

11. Ge, Y., Zhao, L., Cao, J.: Case study of vortex-induced vibration and mitigation mechanism for a long-span suspension bridge. J. Wind Eng. Ind. Aerodyn. **220**, 104866 (2022)

12. Wikipedia contributors: Humen Pearl River Bridge — Wikipedia, The Free Encyclopedia. [Online; accessed 10-July-2023] (2023). https://en.wikipedia.org/w/index.php?title=Humen_Pearl_River_Bridge&oldid=1143100535

13. Simiu, E., Scanlan, R.H.: Wind Effects on Structures: Fundamentals and Applications to Design, 3rd edn. John Wiley & Sons, New Jersey (1996)

14. Basu, R., Vickery, B.: Across-wind vibrations of structure of circular cross-section. part II. development of a mathematical model for full-scale application. J. Wind Eng. Ind. Aerodyn. **12**(1), 75–97 (1983)

15. Sarpkaya, T.: A critical review of the intrinsic nature of vortex-induced vibrations. J. Fluids Struct. **19**(4), 389–447 (2004)

16. Williamson, C., Govardhan, R.: Vortex-induced vibrations. Annu. Rev. Fluid Mech. **36**, 413–455 (2004)

17. Tamura, Y., Amano, A.: Mathematical model for vortex-induced oscillations of continuous systems with circular cross section. J. Wind Eng. Ind. Aerodyn. **14**(1–3), 431–442 (1983)

18. Hartlen, R.T., Currie, I.G.: Lift-oscillator model of vortex-induced vibration. J. Eng. Mech. Div. **96**(5), 577–591 (1970)

19. Ehsan, F., Scanlan, R.H.: Vortex-induced vibrations of flexible bridges. J. Eng. Mech. **116**(6), 1392–1411 (1990)

20. Pol, B., Mark, J.: Frequency demultiplication. Nature **120**(3019), 363–364 (1927)

21. Wu, T., Kareem, A.: Vortex-induced vibration of bridge decks: Volterra series-based model. J. Eng. Mech. **139**(12), 1831–1843 (2013)

22. Xu, K., Ge, Y., Zhao, L., Du, X.: Experimental and numerical study on the dynamic stability of vortex-induced vibration of bridge decks. Int. J. Struct. Stab. Dyn. **18**(03), 1850033 (2018)

23. Xu, K., Ge, Y., Zhao, L.: Quantitative evaluation of empirical models of vortex-induced vibration of bridge decks through sectional model wind tunnel testing. Eng. Struct. **219**, 110860 (2020)

24. Gao, G., Zhu, L., Li, J., Han, W.: Application of a new empirical model of nonlinear self-excited force to torsional vortex-induced vibration and nonlinear flutter of bluff bridge sections. J. Wind Eng. Ind. Aerodyn. **205**, 104313 (2020)

25. Zhang, M., Xu, F., Øiseth, O.: Aerodynamic damping models for vortex-induced vibration of a rectangular 4:1 cylinder: comparison of modeling schemes. J. Wind Eng. Ind. Aerodyn. **205**, 104321 (2020)

26. Liu, P., Chu, X., Cui, W., Zhao, L., Ge, Y.: Bayesian inference based parametric identification of vortex-excited force using on-site measured vibration data on a long-span bridge. Eng. Struct. **266**, 114597 (2022)

27. Zhang, R.-F., Li, M.-C.: Bilinear residual network method for solving the exactly explicit solutions of nonlinear evolution equations. Nonlinear Dyn. **108**(1), 521–531 (2022)

28. Zhang, R.-F., Bilige, S.: Bilinear neural network method to obtain the exact analytical solutions of nonlinear partial differential equations and its application to p-gbkp equation. Nonlinear Dyn. **95**, 3041–3048 (2019)

29. Zhang, R.-F., Li, M.-C., Yin, H.-M.: Rogue wave solutions and the bright and dark solitons of the (3+ 1)-dimensional Jimbo–Miwa equation. Nonlinear Dyn. **103**(1), 1071–1079 (2021)

30. Zhang, R., Bilige, S., Chaolu, T.: Fractal solitons, arbitrary function solutions, exact periodic wave and breathers for a nonlinear partial differential equation by using bilinear neural network method. J. Syst. Sci. Complex. **34**(1), 122–139 (2021)

31. Zhang, R.-F., Li, M.-C., Gan, J.-Y., Li, Q., Lan, Z.-Z.: Novel trial functions and rogue waves of generalized breaking soliton equation via bilinear neural network method. Chaos Solitons Fractals **154**, 111692 (2022)

32. Zhang, R.-F., Li, M.-C., Albishari, M., Zheng, F.-C., Lan, Z.-Z.: Generalized lump solutions, classical lump solutions and rogue waves of the (2+ 1)-dimensional Caudrey-Dodd-Gibbon-Kotera-Sawada-like equation. Appl. Math. Comput. **403**, 126201 (2021)

33. Zhang, R.-F., Li, M.-C., Cherraf, A., Vadyala, S.R.: The interference wave and the bright and dark soliton for two integro-differential equation by using BNNM. Nonlinear Dyn. **111**(9), 8637–8646 (2023)

34. Zhang, R.-F., Bilige, S., Liu, J.-G., Li, M.: Bright-dark solitons and interaction phenomenon for p-gBKP equation by using bilinear neural network method. Phys. Scripta **96**(2), 025224 (2020)

35. Gao, X.-Y.: In the shallow water: Auto-bäcklund, hetero-bäcklund and scaling transformations via a (2+ 1)-dimensional generalized broer-kaup system. Qual. Theory Dyn. Syst. **23**(4), 184 (2024)

36. Gao, X.-Y.: Auto-bäcklund transformation with the solitons and similarity reductions for a generalized nonlinear shallow water wave equation. Qual. Theory Dyn. Syst. **23**(4), 181 (2024)

37. Gao, X.-Y.: Oceanic shallow-water investigations on a generalized Whitham-Broer-Kaup-Boussinesq-Kupershmidt system. Phys. Fluids **35**(12), 127106 (2023)

38. Gao, X.-Y.: Considering the wave processes in oceanography, acoustics and hydrodynamics by means of an extended

coupled (2+ 1)-dimensional burgers system. Chin. J. Phys. **86**, 572–577 (2023)

39. Gao, X.-T., Tian, B.: Water-wave studies on a (2+ 1)-dimensional generalized variable-coefficient Boiti-Leon-Pempinelli system. Appl. Math. Lett. **128**, 107858 (2022)

40. Zhou, T.-Y., Tian, B., Shen, Y., Gao, X.-T.: Auto-bäcklund transformations and soliton solutions on the nonzero background for a (3+ 1)-dimensional Korteweg-de Vries-Calogero-Bogoyavlenskii-Schif equation in a fluid. Nonlinear Dyn. **111**(9), 8647–8658 (2023)

41. Gao, X.-Y.: Two-layer-liquid and lattice considerations through a (3+ 1)-dimensional generalized Yu-Toda-Sasa-Fukuyama system. Appl. Math. Lett. **152**, 109018 (2024)

42. Gao, X.-Y., Guo, Y.-J., Shan, W.-R.: Theoretical investigations on a variable-coefficient generalized forced-perturbed Korteweg-de Vries-Burgers model for a dilated artery, blood vessel or circulatory system with experimental support. Commun. Theor. Phys. **75**(11), 115006 (2023)

43. Wu, X.-H., Gao, Y.-T.: Generalized Darboux transformation and solitons for the Ablowitz–Ladik equation in an electrical lattice. Appl. Math. Lett. **137**, 108476 (2023)

44. Shen, Y., Tian, B., Zhou, T.-Y., Cheng, C.-D.: Multi-pole solitons in an inhomogeneous multi-component nonlinear optical medium. Chaos, Solitons & Fractals **171**, 113497 (2023)

45. Mashnad, M., Jones, N.P.: A model for vortex-induced vibration analysis of long-span bridges. J. Wind Eng. Ind. Aerodyn. **134**, 96–108 (2014)

46. Gao, G., Zhu, L.: Nonlinearity of mechanical damping and stiffness of a spring-suspended sectional model system for wind tunnel tests. J. Sound Vib. **355**, 369–391 (2015)